Recent Decadal Changes in Heat Waves over China: Drivers and Mechanisms

QIN SU

Department of Atmospheric Sciences, Yunnan University, Kunming, China

BUWEN DONG

National Centre for Atmospheric Science–Climate, Department of Meteorology, University of Reading, Reading, United Kingdom

ABSTRACT

Observational analysis indicates significant decadal changes in daytime, nighttime, and compound (both daytime and nighttime) heat waves (HWs) over China across the mid-1990s, featuring a rapid increase in frequency, intensity, and spatial extent. The variations of these observed decadal changes are assessed by the comparison between the present day (PD) of 1994–2011 and the early period (EP) of 1964–81. The compound HWs change most remarkably in all three aspects, with frequency averaged over China in the PD tripling that in the EP and intensity and spatial extent nearly doubling. The daytime and nighttime HWs also change significantly in all three aspects. A set of numerical experiments is used to investigate the drivers and physical processes responsible for the decadal changes of the HWs. Results indicate the predominant role of the anthropogenic forcing, including changes in greenhouse gas (GHG) concentrations and anthropogenic aerosol (AA) emissions in the HW decadal changes. The GHG changes have dominant impacts on the three types of HWs, while the AA changes make significant influences on daytime HWs. The GHG changes increase the frequency, intensity, and spatial extent of the three types of HWs over China both directly via the strengthened greenhouse effect and indirectly via land–atmosphere and circulation feedbacks in which GHG-change-induced warming in sea surface temperature plays an important role. The AA changes decrease the frequency and intensity of daytime HWs over Southeastern China through mainly aerosol–radiation interaction, but increase the frequency and intensity of daytime HWs over Northeastern China through AA-change-induced surface–atmosphere feedbacks and dynamical changes related to weakened East Asian summer monsoon.

1. Introduction

Heat waves, commonly defined as prolonged periods of excessive hot weather, are a distinctive type of high-temperature extreme (Perkins and Alexander 2013; Perkins 2015). These high-temperature extremes show increasing occurrence in recent decades as the global mean temperature rises (e.g., Alexander et al. 2006; Donat et al. 2013), leading to severe damage to human society and ecosystems (e.g., Meehl and Tebaldi 2004; Fischer et al. 2007; Coumou and Rahmstorf 2012; Seneviratne et al. 2014; Sun et al. 2014). For instance, the extreme long-lasting heat wave over Europe during the summer of 2003 caused about 66 000 deaths (e.g., Schär and Jendritzky 2004; Robine et al. 2008), and the record-breaking heat wave over western Russia during July 2010 yielded a death toll of 11 000 and grain harvest losses of 30% (e.g., Coumou and Rahmstorf 2012; Matsueda 2011). The disastrous impact of heat waves on human lives, agriculture, and economies highlights the urgency of understanding the changes of heat waves and associated physical processes.

Since the mid-1990s, heat waves have become more frequent and severe across China (You et al. 2017; Li et al. 2017; Luo and Lau 2017; Wang et al. 2017; Freychet et al. 2018a). Several devastating heat waves in recent decades, such as the July–August 2013 heat wave in Central and Eastern China and the 2015 summer heat wave in Western China, have caused considerable damage to agricultural production and human health (e.g., Sun et al. 2016; Ma et al. 2017). The July–August

---

Corresponding author: Qin Su, suqin@ynu.edu.cn

2013 heat wave in Central and Eastern China lasted more than 30 days (Zhou et al. 2014; Ma et al. 2017), and the regionally averaged surface air temperature broke the historical record, exceeding the observed 1961–90 climatology by 1.89°C. The 2015 summer registered the hottest summer over Western China, with the area-averaged summer daily mean, maximum, and minimum surface air temperatures breaking the historical records (Sun et al. 2016). In addition, Northeastern China experienced a hot summer in 2014, which was associated with decrease in precipitation (Wilcox et al. 2015a).

Previous studies demonstrated a crucial role of anthropogenic activity in increasing the occurrence of the extreme temperatures and long-lasting heat waves over China (Wen et al. 2013; Sun et al. 2014; Lu et al. 2016; Freychet et al. 2017, 2018a,b; Chen and Dong 2019), as well as intensifying the magnitude of the extreme temperatures (Yin et al. 2017). Most of those studies focused on all combined anthropogenic impact, rather than the individual effect of anthropogenic forcing. For instance, the individual role of changes in greenhouse gases concentrations (GHG) and anthropogenic aerosol (AA) emissions in the changes of long-lasting heat waves are not clear.

Different anthropogenic forcings influence the atmospheric temperature through distinct thermodynamic and dynamical processes, but the mechanisms related to the responses of heat waves (HWs) to different anthropogenic forcings have not yet been fully understood. The increase in GHG concentrations warms the atmosphere by absorbing more outgoing longwave radiation (e.g., Cubasch et al. 2001; Dong et al. 2009). At the same time, the atmospheric temperature is also affected by the circulation changes due to the GHG concentration changes. The increased GHG concentrations enhance the southern part of the East Asian summer monsoon (EASM) circulation, which results from the competing effects of the increase in moisture static energy related to the strengthened land–sea thermal contrast and the midtroposphere convective barrier associated with reduced relative humidity in a warming world (Lau and Kim 2017; Lau et al. 2017). In addition, the strengthened land–sea thermal contrast is determined by the direct GHG radiative effect (Li and Ting 2017; Tian et al. 2018). The changes of AA emissions affect the surface and atmospheric temperature by directly scattering and absorbing the solar radiation through aerosol–radiation interaction and by changing the cloud properties through aerosol–cloud interaction (e.g., Rosenfeld et al. 2008; Stevens and Feingold 2009; Tao et al. 2012; Li et al. 2016b). Both the local AA emission changes and the remote AA emission changes have an impact on the summer extreme temperatures over China through aerosol change-induced precipitation–soil moisture–cloud–temperature feedbacks (Dong et al. 2016a,b). Local summer warming associated with reduced precipitation leads to a decrease in evaporation and less cloud cover since the precipitation deficit induces drying soil. Increased solar radiation at the surface associated with less cloud cover and decreased upward latent heat fluxes associated with reduced evaporation cause a positive feedback to the surface warming. Moreover, the dynamical feedbacks of the reduced EASM circulation and rainfall, which, induced by the weakened land–sea thermal contrast and more stable atmosphere in response to the increase in AA emissions, could also have an impact on atmospheric temperature (Guo et al. 2013; Li et al. 2016b, 2018b; Tian et al. 2018).

Up to now, the heat waves are precisely classified into three categories (e.g., Chen and Li 2017; Chen and Zhai 2017): daytime (only hot in day), nighttime (only hot at night), and compound ones (hot in both day and night), since extreme high temperature at night, inducing great heat-related morbidity and mortality (Hajat et al. 2006; Gosling et al. 2009), is as disastrous as that in daytime. These three types of heat waves are of different features and associated with different mechanisms (e.g., Chen and Li 2017; Chen and Zhai 2017; Hong et al. 2018). However, most of the previous studies focused on the characteristics and changes of daytime heat waves (e.g., Ding et al. 2010; Guo et al. 2017; Luo and Lau 2017; Lu and Chen 2016; Wang et al. 2017). The changes of compound and nighttime heat waves, especially the drivers and physical mechanisms for the recent decadal change, are not well understood (You et al. 2017; Li et al. 2017; Luo and Lau 2017). Also, the individual contributions of changes in GHG concentrations and AA emissions to the recent decadal changes in heat waves are not evaluated and the associated physical processes are not revealed yet, since the previous studies assessed all anthropogenic impacts together (e.g., Sun et al. 2016; Ma et al. 2017). Therefore, the main aims of this work are to revisit the time evolutions in the three types of heat waves over China in observations with a focus on the recent decadal changes across the mid-1990s, to quantify the relative roles of changes in GHG concentrations and AA emissions in shaping these decadal changes, and to understand the associated physical processes.

The structure of this paper is organized as follows: The observed decadal changes in heat waves over China are revisited in section 2. The model and experiments are described briefly in section 3. The simulated changes in response to different changes in anthropogenic forcings are shown in section 4. The physical processes responsible for simulated changes in heat waves forced by

different anthropogenic forcings, such as GHG concentrations and AA emissions, are illustrated in section 5. Conclusions are summarized in section 6.

2. Observed decadal changes in heat waves over China

a. Observational datasets

Observations used in this are the homogenized datasets of daily maximum temperature T_{max} and minimum temperature T_{min} at 753 stations over China during 1960–2013 (Li et al. 2016a). Regarding the distinct local climate in China, the HWs over three subregions are also analyzed, which are Southeastern China (SEC, south of 35°N and east of 105°E), Northeastern China (NEC, north of 35°N and east of 105°E), and Western China (WC, west of 105°E). There are 334, 224, and 195 stations in SEC, NEC, and WC, respectively (Fig. 2g shows the distributions of the stations over these three subregions). This study focuses on the extended summer (May–September) HWs.

b. Definition of HWs

A HW is defined as a weather event with daily temperature exceeding a threshold continuously for a few days (e.g., Perkins and Alexander 2013). Both absolute and relative thresholds could be used to define a heat wave. The absolute threshold is a fixed temperature value, such as 35°C (e.g., Tan et al. 2007; Sun et al. 2014), while the relative threshold is decided by local climate, varying at different places on different dates (Stefanon et al. 2012). Concerning the various climate types in China, the relative threshold is employed to define the heat waves in this study and it has also been widely used in some previous studies (e.g., Li et al. 2017; Wang et al. 2017). The relative threshold on each calendar day is calculated as the daily 90th percentile of T_{max} or T_{min} based on 15-day samples centered on that day during the baseline period of 1964–81 (i.e., total samples $15 \times 18 = 270$ days; Della-Marta et al. 2007). A HW is defined when the daily temperature is higher than the relative threshold for at least 3 days. All the HWs are categorized as three independent types:

1) Compound HW—at least *three* consecutive days with simultaneous hot days and hot nights ($T_{max} \geq$ 90th percentile and $T_{min} \geq$ 90th percentile).
2) Daytime HW—at least *three* consecutive hot days (only $T_{max} \geq$ 90th percentile), without consecutive hot nights.
3) Nighttime HW—at least *three* consecutive hot nights (only $T_{min} \geq$ 90th percentile), without consecutive hot days.

Three indicators, that is, frequency, intensity, and spatial extent, are used to measure the HWs in a year. The frequency is represented by the accumulated occurrence of events within a year. The intensity of each event is calculated by averaging the everyday temperature anomalies within an event, which are obtained by subtracting the corresponding threshold from the daily temperatures. Particularly, the intensity of compound HWs is the sum of the averaged T_{max} and T_{min} anomalies. The intensity for a year is computed by averaging the intensity of events occurring in that year. The spatial extent is calculated through a "frozen grid" scheme (Jones et al. 1986). The mainland of China is divided into 1.875° longitude $\times$ 1.25° latitude boxes, with a total number of N. There are $n(i)$ stations in total situated in box i, in which $nh(i, t)$ stations experience at least one extreme event during the extended summer in year t. Then the spatial extent in year t is computed as $\sum_{i=0}^{i=N}[nh(i, t)/n(i)] \times 1.875 \times 110 \times 1.25 \times 110$, in which "110" denotes an approximate distance per unit longitude/latitude.

c. Observed decadal change

Figure 1 shows the time evolution of the area-averaged frequency and intensity as well as the spatial extent of the compound, daytime, and nighttime HWs. The time series of the three properties of compound and nighttime HWs seems to be dominated by linear trends on low-frequency time scales, while those of daytime HWs are featured by abrupt decadal changes. These could be attributed to that the changes in compound and nighttime HWs are predominantly contributed to by the changes of GHG concentrations, which show an increasing trend (Le Quéré et al. 2009), and the changes in daytime HWs are partly influenced by the AA changes, which show significant decadal changes across mid-1990s (Lamarque et al. 2010), which are indicated by the results in section 4. Interestingly, the frequency and intensity of one type of HWs are highly correlated with the correlation coefficient for all of China of 0.90, indicating highly coupled interannual variations of frequency and intensity of one type of HWs. However, the interannual variations are not the concern of this study, which will not be explored more in this paper.

All three type HWs over China experienced an abrupt decadal change across the mid-1990s, characterized by increases in frequency, intensity, and spatial extent (Fig. 1). These rapid decadal changes are robust features, and they are not sensitive to the baseline period used to find the relative thresholds and define HWs. In the rest of this paper, HWs are defined using the relative thresholds based on the period of 1964–81. Compared with daytime and nighttime HWs, compound HWs
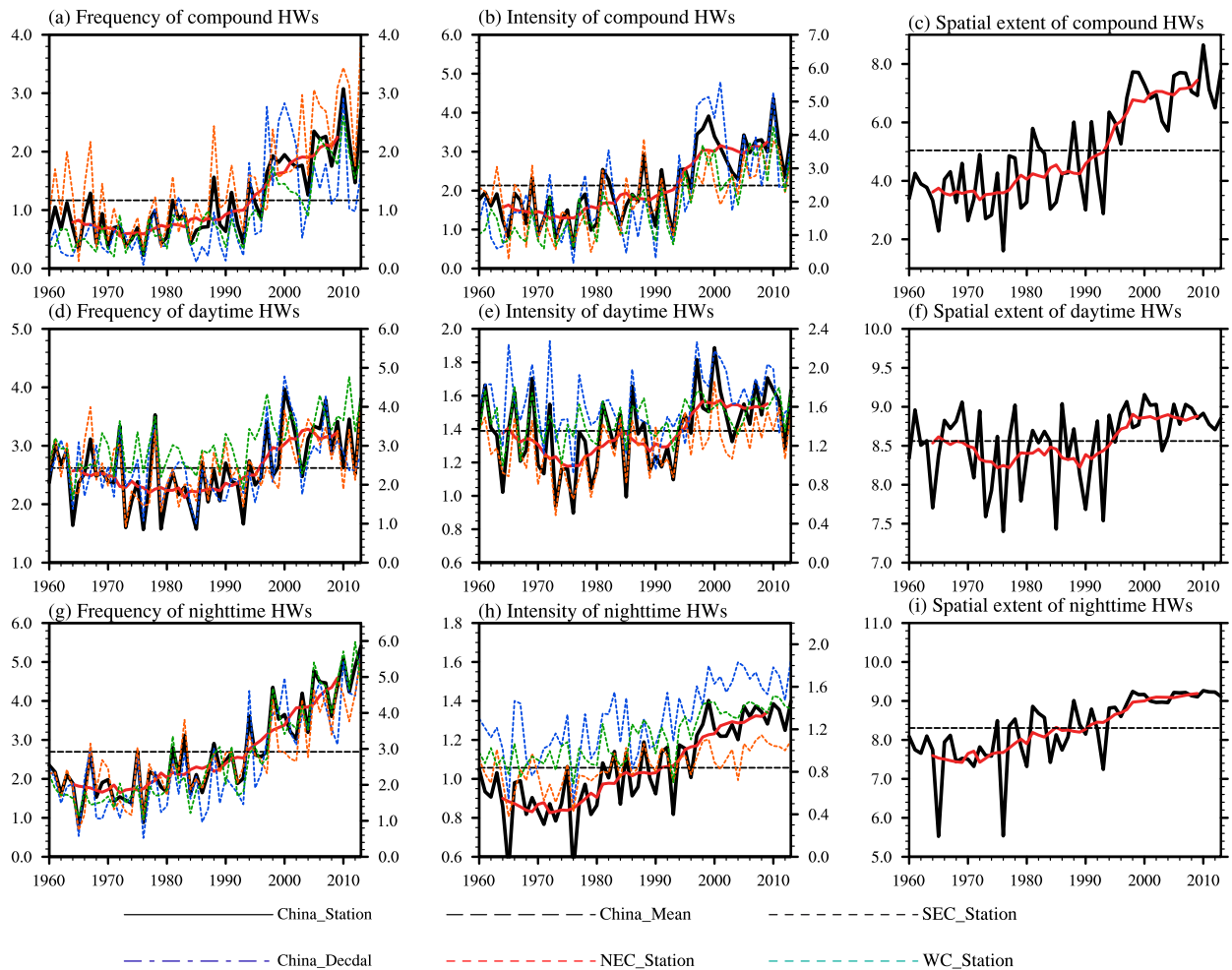
FIG. 1. Time series of area-averaged (left) frequency (events per year), (center) intensity (°C), and (right) spatial extent (10^6 km^2) of (a)–(c) compound, (d)–(f) daytime, and (g)–(i) nighttime HWs in extended summer over the whole mainland of China (black solid lines), Northeastern China (blue dashed lines), Southeastern China (orange dashed lines), and Western China (green dashed lines). Black dashed lines denote the time means of area-averaged indicators. Red solid lines represent the decadal variations of area-averaged indicators, obtained by a 9-yr running average. The black solid and dashed, as well as the red solid lines are for the left Y axis, while the dashed blue, orange, and green lines are for the right Y axis.

exhibited the most dramatic changes in all three aspects. The frequency of compound HWs during 1994–2011 [present day (PD)] is almost triple that during 1964–81 [early period (EP)], rising from 0.67 events per year to 1.85 events per year (Table 1). These two periods were chosen to avoid years with a strong impact of volcanic eruptions (Dong et al. 2017). The intensity of compound HWs doubled the value of the EP after mid-1990s, with the value changing from 1.42° to 3.09°C (Table 1). The spatial extent of compound HWs expanded from 3.66 × 10^6 to 6.97 × 10^6 km^2 (Table 1). The decadal changes of daytime HWs show some similar features in comparison with the compound ones, but with relatively small magnitude. The frequency and intensity of daytime HWs increased by 0.7 events per year and 0.29°C

(Table 1). The spatial extent expanded from 8.38 × 10^6 to 8.86 × 10^6 km^2 (Table 1) compared to the whole China area of 9.63 × 10^6 km^2. The nighttime HWs also showed decadal increases in all three aspects. The

TABLE 1. Area-averaged decadal changes of the properties for the three types of HWs over China in observations.

	Frequency (events per year)		Intensity (°C)		Spatial extent (10^6 km^2)	
	EP	PD	EP	PD	EP	PD
Compound HWs	0.67	1.85	1.42	3.09	3.66	6.97
Daytime HWs	2.36	3.06	1.26	1.55	8.39	8.86
Nighttime HWs	1.80	3.76	0.86	1.27	7.61	9.06

frequency of nighttime HWs exhibited a sharp increase across the mid-1990s, changing from 1.76 events per year to 3.72 events per year, which means that there are on average two more nighttime HWs over China in every summer during the PD relative to the EP (Table 1). The intensity of nighttime HWs enhanced significantly by 0.41°C (Table 1). The influencing area increased by about 20% (Table 1). In addition, the frequency and intensity of the three types of HWs averaged over the three subregions show similar rapid decadal changes as those averaged over all of China. Moreover, all the area-averaged changes above are calculated based on station data. The area-averaged changes are also computed after interpolating station data to regular grids, and they are nearly identical to the ones based on station data.

Figure 2 illustrates the spatial patterns of the decadal changes in frequency and intensity of the three types of HWs over China across the mid-1990s in observations. Nearly all the decadal changes in each indicator of the three types of HWs are positive throughout China, but with different spatial patterns. The occurrence of compound HWs increased the most over the northern part of China, mid–lower reaches of the Yangtze River, and the delta of the Pearl River, with an increase in frequency of more than 2.0 events per year (Fig. 2a). The changes of intensity of compound HWs share a similar spatial distribution with the frequency (Fig. 2b), with the maximum of intensity changes located at the northern part of China (about 4.8°C). The spatial patterns of changes in frequency and intensity for daytime and nighttime HWs show some distinct features with increases in both frequency and intensity for nighttime HWs being stronger than those for daytime HWs (Figs. 2c–f). The significant increase in frequency of daytime HWs primarily appeared in the northern part of China, especially in the western part of China with a value of about 2.5 events per year (Fig. 2c), while the significant intensification in magnitude of daytime HWs of around 0.6°C mainly occurred in the central part of China (Fig. 2d). The frequency of nighttime HWs increased significantly in the northern part of China (Fig. 2e), with a range of 1.5–3.0 events per year. The largest increase is situated on the south flank of the Tibetan Plateau with the maximum of 6.2 events per year. The intensity of the nighttime HWs is significantly enhanced in the northern part of China (Fig. 2f), with the maximum of 1.1°C. Interestingly, the nighttime HWs in Central-Eastern China exhibited a large increase in frequency and intensity, while the daytime HWs over there showed the opposite changes, with frequency decreasing and intensity weakening slightly and the compound HWs over there displayed little changes. Previous studies investigating the linear trends of the HWs also reported similar changes in these

three types of HWs in Central-Eastern China (Ding et al. 2010; Chen and Li 2017; Freychet et al. 2017). However, the physical mechanism for the trends in these three type HWs is still not clear.

3. Model and experiments design

The above results show that the observed three types of HWs exhibited significant decadal changes across the mid-1990s. A set of numerical experiments is performed to assess whether the anthropogenic forcings (GHG concentrations and AA emissions) contribute to these decadal changes in observations, and what the relative roles of the individual forcings are, and what the main physical processes involved are.

a. Model and experiments design

This study used an atmosphere–ocean–mixed layer coupled model, the Met Office Unified Model–Global Ocean Mixed Layer 1 (MetUM-GOML1; Hirons et al. 2015), by performing a set of numerical experiments to estimate the contributions of combined GHG and AA changes or individual forcing change on the decadal changes of three type HWs in China. MetUM-GOML1 is a coupled model comprising the atmosphere component of the Met Office Unified Model at the fixed scientific configuration Global Atmosphere 3.0 (GA3.0; Arribas et al. 2011; Walters et al. 2011) and a multicolumn K-profile parameterization (MC-KPP) mixed layer ocean model. The vertical MC-KPP columns are configured over 100 levels within a depth of 1000 m using a stretch function, so the vertical resolution of MC-KPP is 1.2 m at the surface and about 2 m over the first 41.5 m near the surface. Since MC-KPP includes only vertical mixing processes and does not include ocean dynamics, the corrections of temperature and salinity are applied. In the corrections, the mean ocean advections are represented by the prescribed seasonally varying 3D temperature and salinity fluxes, which also account for the biases in atmospheric surface heat and freshwater fluxes. The frequency of coupling between atmospheric and oceanic components is once every 3 h. The advantages of this atmosphere–ocean–mixed layer coupled model are less computational time and smaller biases in simulated sea surface temperature than the fully coupled ones (Hirons et al. 2015; Dong et al. 2017; Luo et al. 2019). All experiments are run at the horizontal resolution of 1.875° longitude × 1.25° latitude with 85 vertical levels in the atmosphere.

Table 2 summarizes the performed experiments in this study. First of all, a relaxation experiment (R0) for 12 years was performed. In the relaxation experiment, the PD GHG and AA forcings (Lamarque et al. 2010, 2011)
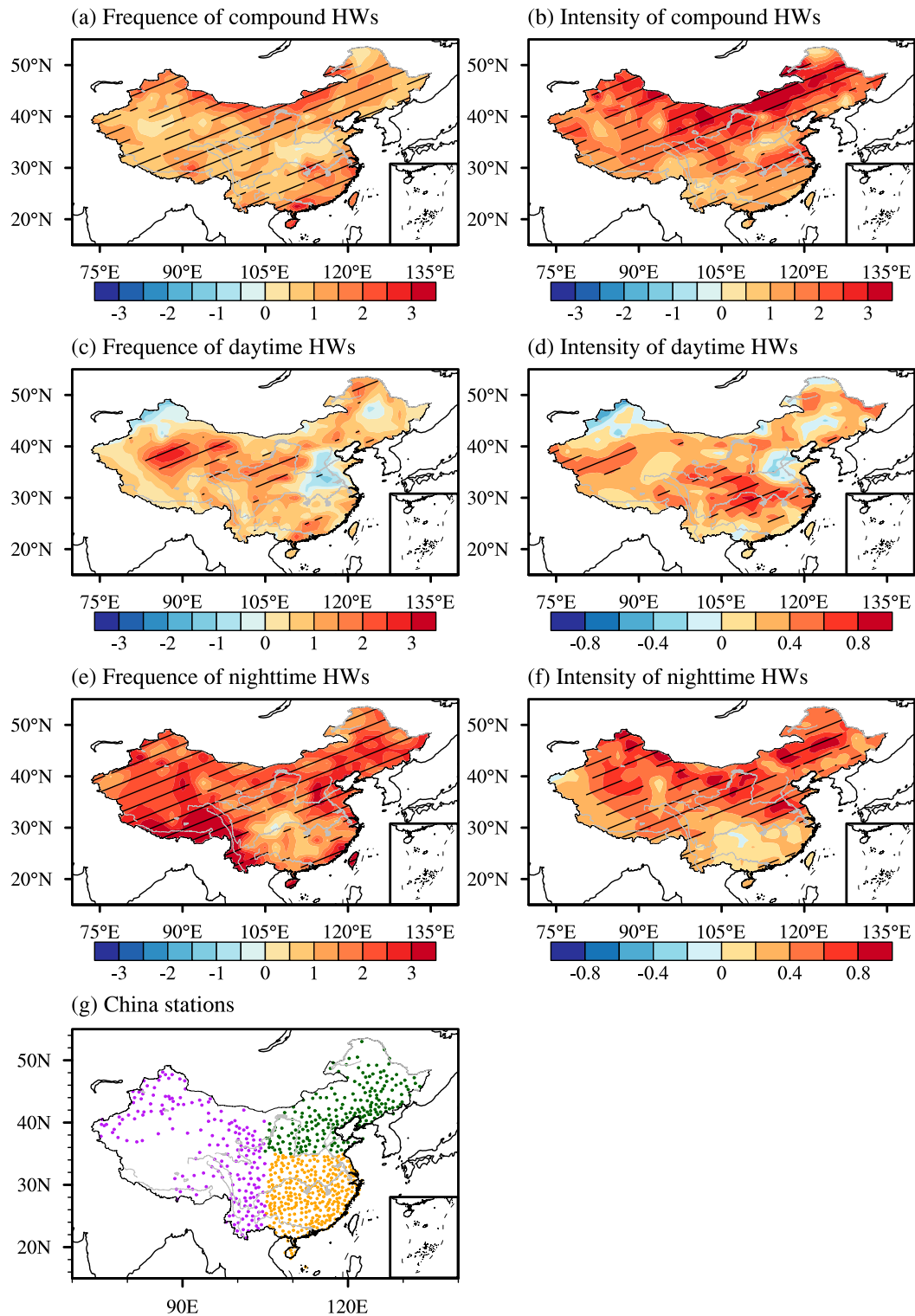
FIG. 2. Spatial patterns of differences in (left) frequency (events per year) and (right) intensity (°C) of (a),(b) compound, (c),(d) daytime, and (e),(f) nighttime HWs between the PD and EP. The slashes highlight the regions where the changes are statistically significant at the 90% confidence level based on a two-tailed Student's *t* test. (g) Distributions of 753 stations in the China station dataset. The three subregional groups are marked with different color dots. The dots in green, orange, and purple represent the subregions of NEC, SEC, and WC, respectively.

TABLE 2. Summary of numerical experiments. Note that a slightly different period of 1970–81 for the aerosol forcing in the EP is used since aerosol emissions data before 1970 were not available.

Abbreviation	Experiment	Ocean	Radiative forcing
R0	Relaxation run	Relaxation to "present day" (PD, 1994–2011) mean 3D ocean temperature and salinity to diagnose climatological temperature and salinity tendencies	PD GHGs over 1994–2011 and AA emissions over 1994–2010 with AA after 2006 from RCP4.5 scenario (Lamarque et al. 2010, 2011)
C-EP	EP (1964–81)	Climatological temperature and salinity tendencies from relaxation run	EP mean GHG and EP mean AA emissions
C-PD	PD (1994–2011) with GHG and AA forcings		PD mean GHG and PD mean AA emissions
C-PD-GHG	PD (1994–2011) with GHG forcing		PD mean GHG and EP mean AA emissions
C-PD-AA	PD (1994–2011) with AA forcing		EP mean GHG and PD mean AA emissions

are used and the ocean temperature and salinity were relaxed to a PD (1994–2011) climatology, which is derived from the Met Office ocean analysis (Smith and Murphy 2007). The climatological seasonal cycle of daily mean 3D ocean temperature and salinity corrections are obtained from the relaxation experiment. These ocean temperature and salinity corrections are then applied to the free-running coupled experiments. Four other time-sliced experiments are performed by using different forcings, that is, the C-EP experiment forced by the EP (1964–81) mean GHG concentrations and appropriate AA emissions, the C-PD experiment forced by the PD (1994–2011) mean GHG concentrations and AA emissions, the C-PD-GHG experiment forced by the PD mean GHG concentrations, but the appropriate EP mean AA emissions, and the C-PD-AA experiment forced by the PD mean AA emissions, but the EP mean GHG concentrations. All experiments are run for 50 years and use the climatological PD sea ice extent from HadISST (Rayner et al. 2003). The same set of experiments was used to investigate the forced decadal summer precipitation change over East Asia in Tian et al. (2018) and the decadal changes of temperature extremes over China in Chen and Dong (2019). The last 45 years of each experiment are used for analysis. The HWs in the experiments are defined the same way as in observations, except that the relative threshold on each day is calculated as the daily 90th percentile of $T_{\max}$ or $T_{\min}$ based on 15-day samples centered on this day during the last 45 years of the C-EP experiment (i.e., total samples $15 \times 45 = 675$ days). The difference between a pair of experiments that include and exclude a particular forcing indicates the response to that forcing. The difference between C-PD and C-EP indicates the combined effect of changes in both GHG concentrations and AA emissions (hereafter ALL forcing). The impact of changes in GHG concentrations (hereafter GHG forcing) is the

difference between C-PD-GHG and C-EP and the impact of changes in AA emissions (hereafter AA forcing) is the difference between C-PD-AA and C-EP. Statistical significance of the mean changes is assessed using a two-tailed Student's t test.

b. Model climate for $T_{\max}$ and $T_{\min}$

The climatological means of $T_{\max}$ and $T_{\min}$ in the C-PD experiment for the extended summer are compared with the observed ones during PD (Fig. 3). The observed $T_{\max}$ means show more or less uniform distributions over the southeastern part of China, with values higher than 29°C, decreasing northward with values about 23°–26°C over the northeastern part of China. Over Western China, a low-value center is located over the Tibetan Plateau and a high-value center over the northwestern part of China with temperatures above 29°C (Fig. 3a). The climatological means of observed $T_{\min}$ exhibit a large meridional gradient over the eastern part of China, with the maximum higher than 23°C on the southeast coast of China and a minimum of 8°–11°C over Northeast China. The spatial distribution of $T_{\min}$ over Western China shows a minimum (less than 2°C) over the Tibetan Plateau and a high value (14°–20°C) over the northwestern part of China, which is similar to the spatial pattern in $T_{\max}$ (Fig. 3b). The spatial patterns of climatological extended-summer means of $T_{\max}$ and $T_{\min}$ in the C-PD experiment and regional magnitudes agree well with the observed ones, with pattern correlation coefficients of 0.82 for $T_{\max}$ and 0.88 for $T_{\min}$ (Figs. 3c,d). The observed $T_{\max}$ distributions are reproduced by the model over the southeastern and northwestern parts of China with a value above 29°C, but they are slightly underestimated over the Tibetan Plateau and northeastern part of China (Fig. 3d). The observed $T_{\min}$ distributions are also well simulated by the model, with some underestimation over the Tibetan Plateau (Fig. 3c). These
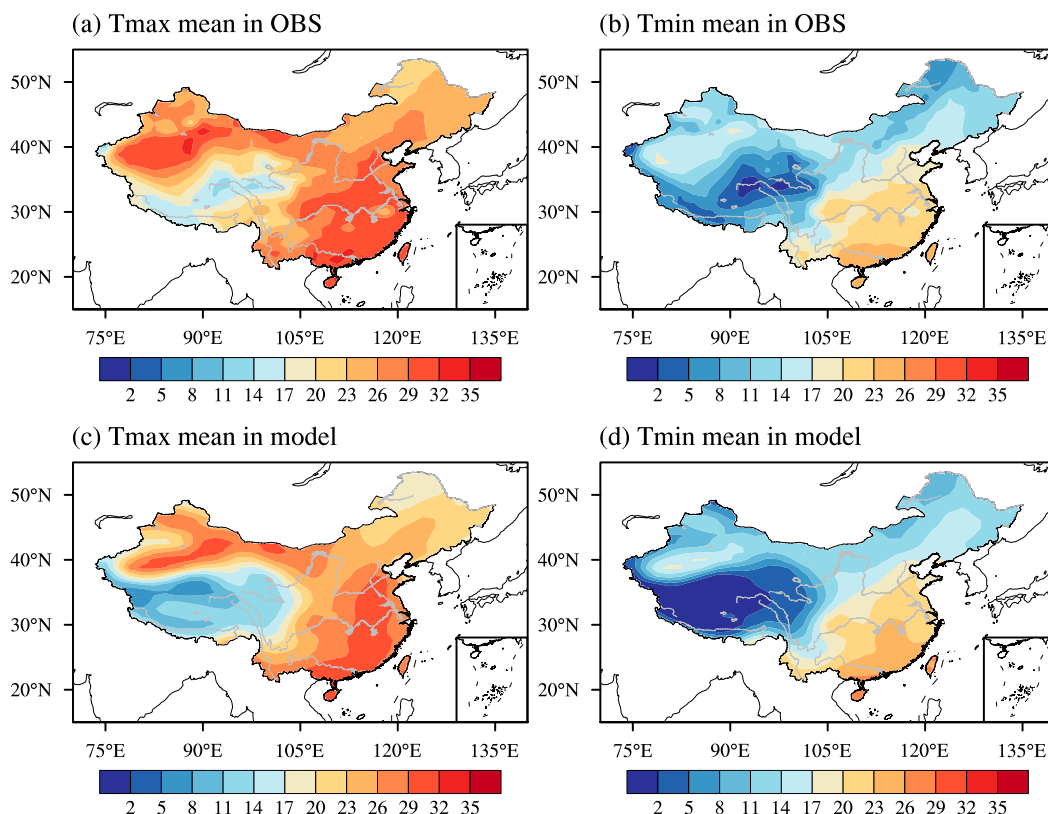
FIG. 3. Climatological means of extended-summer-mean (May–September) T_{max} and T_{min} (°C) during the PD (1994–2011) (a),(b) in observations and (c),(d) in the C-PD experiment.

results indicate that the model reproduce many features of the extended-summer climatological means of T_{max} and T_{min} in observations, suggesting that the model used in this study is appropriate for investigating the response of the temperature extremes related to HWs to different anthropogenic forcings.

4. Model simulated responses to different anthropogenic forcings

a. Spatial pattern of responses to different forcings

Figure 4 shows the spatial patterns of changes in frequency and intensity of the compound HWs in response to different anthropogenic forcings in model experiments. The significant increases in the frequency and intensity throughout China and their spatial distributions in observations (Figs. 2a,b) are well reproduced by the ALL forcing experiment (Figs. 4a,b). The spatial patterns of the increases in the model experiment are consistent with the observed ones with a relatively large increase in frequency and strong enhancement in intensity over the northern part of China and mid–lower reaches of Yangtze River, though the magnitudes of the

changes in response to ALL forcing for increases in frequency are smaller than the observed ones. These results demonstrate that the observed decadal increases in occurrence and intensity of compound HWs over China across the mid-1990s are predominantly attributed to the anthropogenic GHG and AA changes.

Furthermore, the changes of compound HWs in response to GHG forcing share very similar patterns with the changes in the ALL forcing experiment (Figs. 4c,d), while the changes driven by the AA forcing are relatively weak, except for some local significant decreases in frequency and intensity over SEC (Figs. 4e,f). Thus, comparing the responses to only GHG with those to only AA changes indicates that the GHG changes play a dominant role in the increase in frequency and intensity of compound HWs. In addition, the model overestimates the increase in frequency of compound HWs over the southwestern part of China, which results from the GHG impact (Figs. 2a and 4a,c).

The changes of daytime HWs in response to the different forcings are shown in Fig. 5. The principal features of the changes of daytime HWs in the ALL forcing experiment are significant increases in frequency and intensity over the northern part of China (Figs. 5a,b).
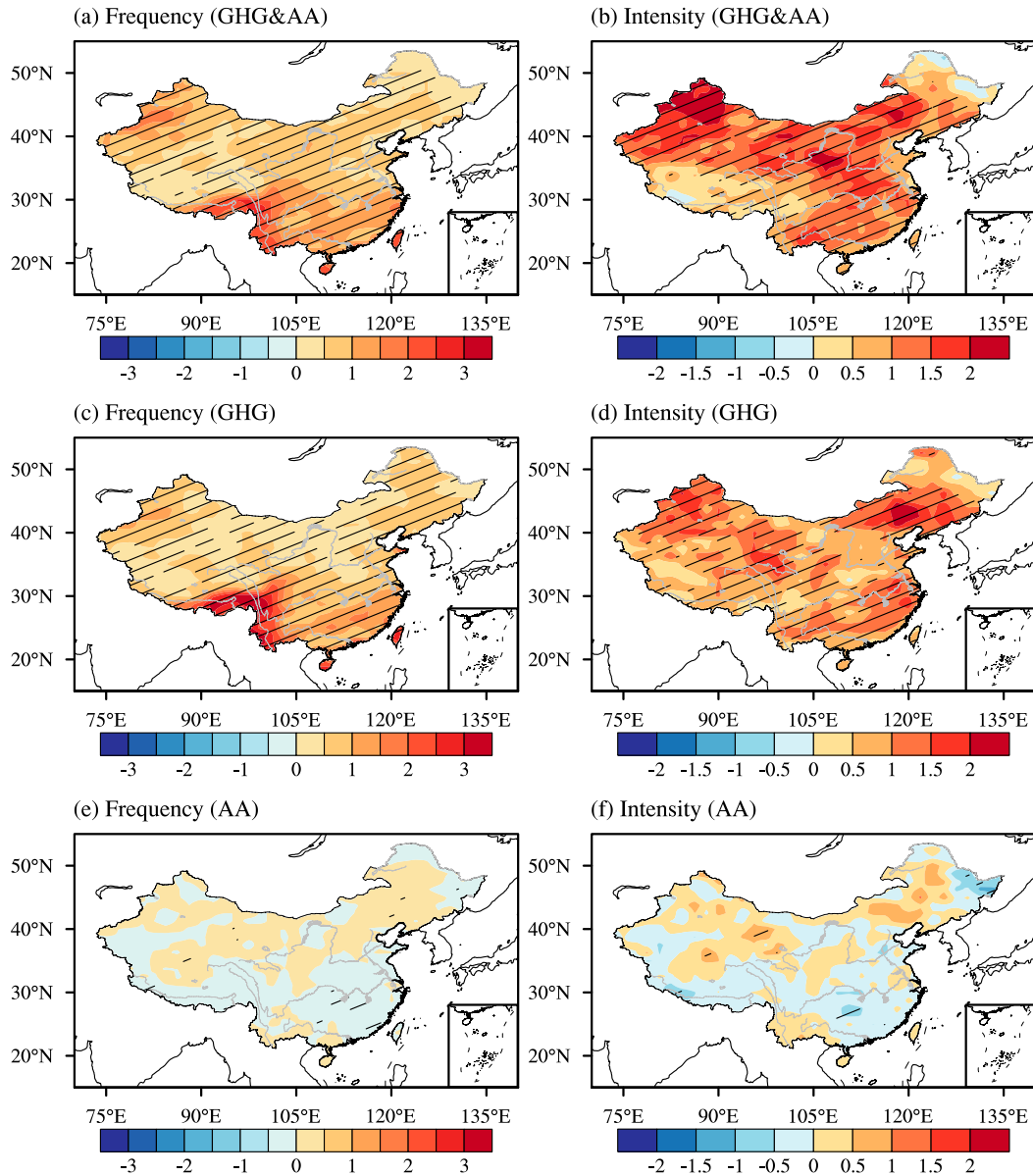
FIG. 4. Spatial patterns of changes in (left) frequency (events per year) and (right) intensity (°C) of compound HWs in response to changes in (a),(b) ALL forcing, (c),(d) GHG forcing, and (e),(f) AA forcing, masked by the China boundary. The slashes highlight the regions where the differences are statistically significant at the 90% confidence level based on a two-tailed Student's t test.

These main features show some similarities with the observed changes (Figs. 2c,d). However, the changes in the intensity of daytime HWs over the northern part of China are overestimated, but those over the central part of China are underestimated. Both the GHG and AA forcing changes are important to the changes of daytime HWs. Responses to the GHG forcing share similar spatial patterns with those in the ALL forcing experiment, with a small difference in the magnitude of changes, indicating the dominant role of GHG changes

in affecting the daytime HWs (Figs. 5c,d). Changes of the daytime HWs induced by the AA impact exhibit dipole patterns over China, with increases over northern China and decreases or weak changes over southern China (Figs. 5e,f). In addition, the responses to AA forcing are of more significance for daytime HWs than for compound HWs, implying greater AA impact on the daytime HWs.

Responses of the nighttime HWs to the different forcings are shown in Fig. 6. In comparison with
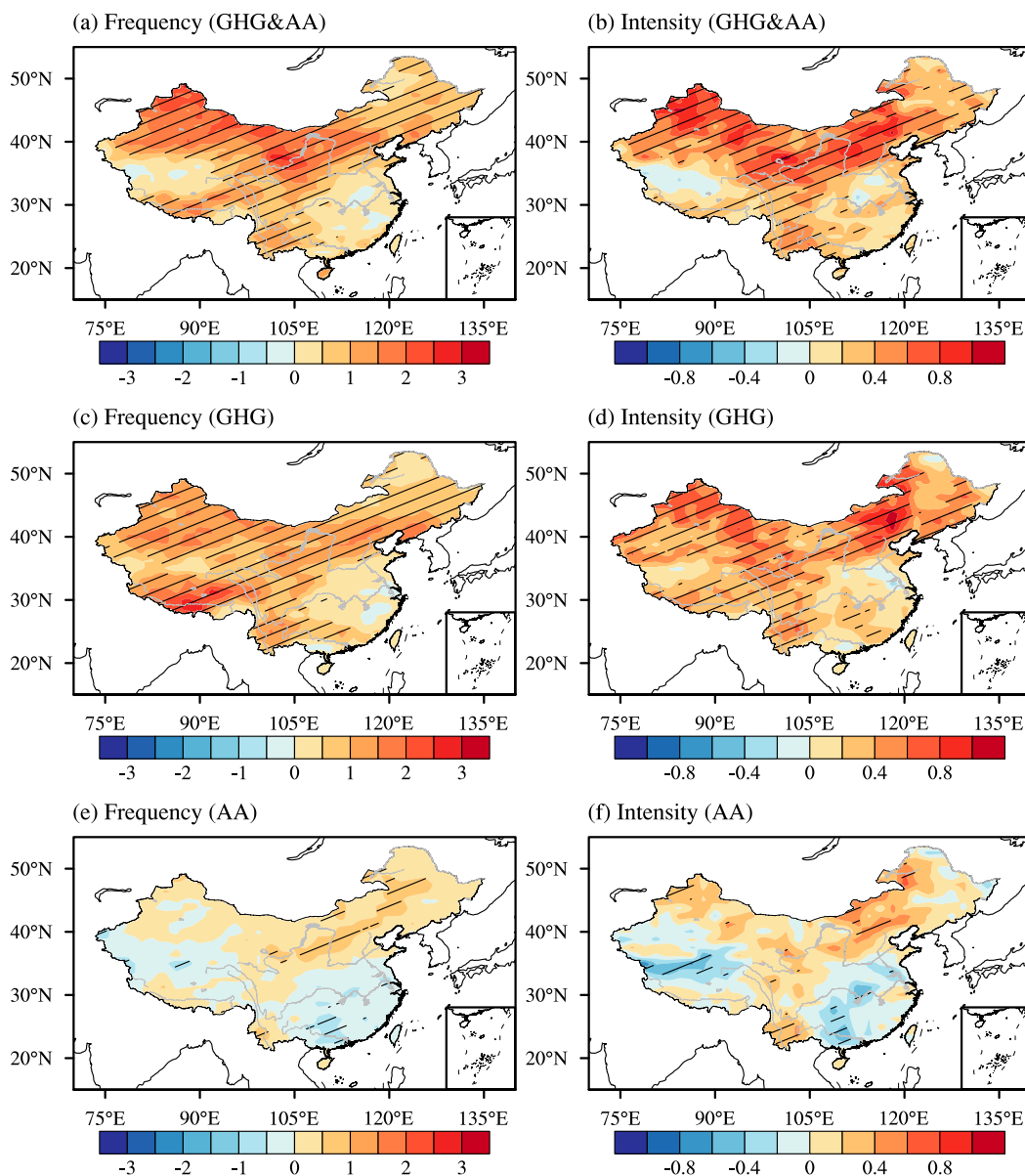
FIG. 5. Spatial patterns of changes in (left) frequency (events per year) and (right) intensity (°C) of daytime HWs in response to changes in (a),(b) ALL forcing, (c),(d) GHG forcing, and (e),(f) AA forcing, masked by the China boundary. The slashes highlight the regions where the differences are statistically significant at the 90% confidence level based on a two-tailed Student's *t* test.

observed changes shown in Fig. 2, the model reproduces significant increases in the frequency and intensity of the nighttime HWs over the northern part of China in response to ALL forcing changes (Figs. 6a,b). Comparison between responses to different forcings illustrates that the significant changes of the nighttime HWs in the model simulations are primarily due to the GHG changes (Figs. 6c,d) with impacts of changes in AA being generally weak (Figs. 6e,f). Additionally, the increases in frequency over the southeastern part of China

are overestimated because the GHG changes induce strong increases there, but the AA changes result in weak decreases.

b. Area-averaged responses to different forcings

The area-averaged changes in frequency and intensity and changes in the spatial extent of the three types of HWs over all of China and all three subregions for both observations and model experiments are demonstrated in Fig. 7. Quantitatively, the changes of the three types
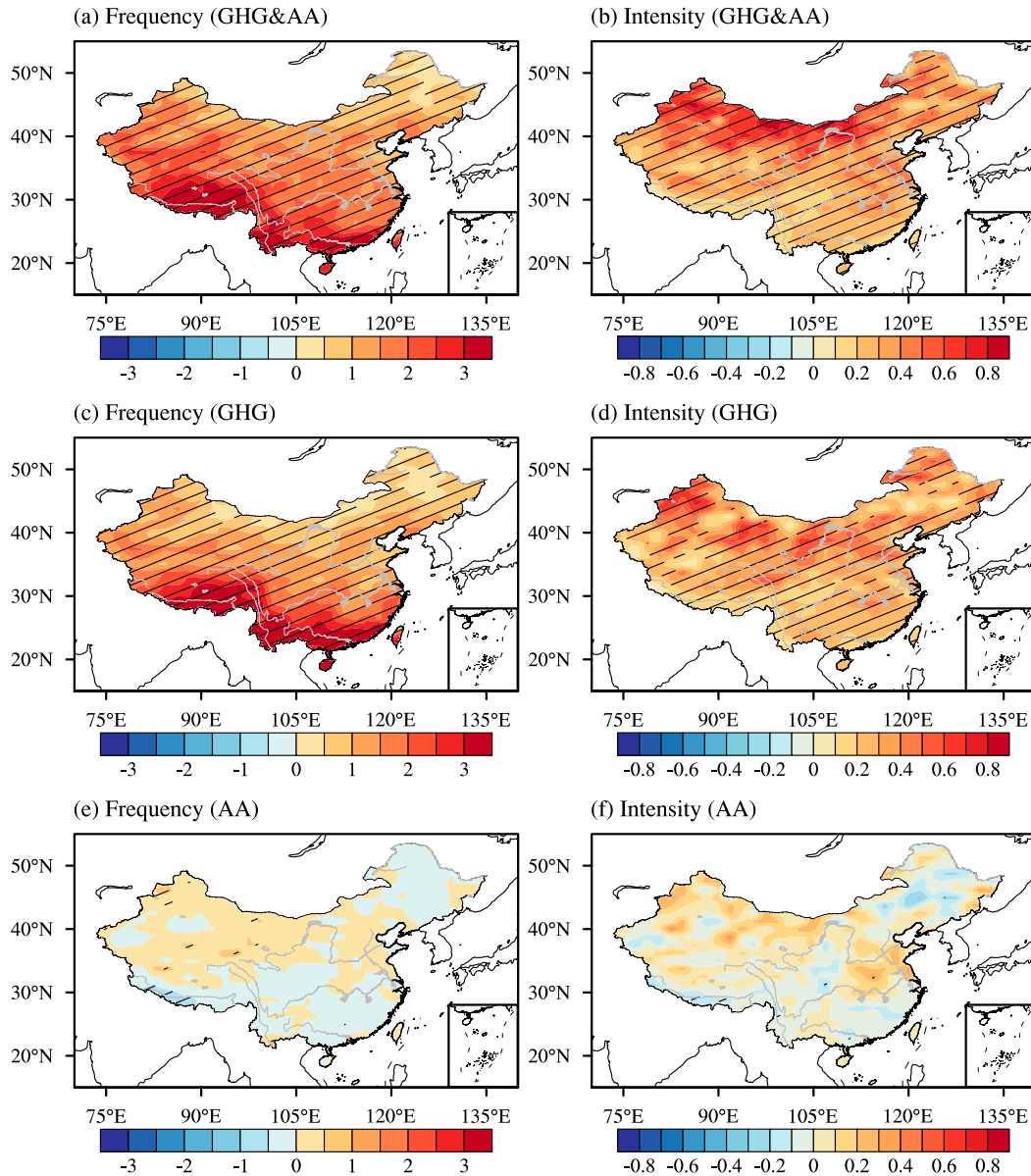
FIG. 6. Spatial patterns of changes in (left) frequency (events per year) and (right) intensity (°C) of nighttime HWs in response to changes in (a),(b) ALL forcing, (c),(d) GHG forcing, and (e),(f) AA forcing, masked by the China boundary. The slashes highlight the regions where the differences are statistically significant at the 90% confidence level based on a two-tailed Student's *t* test.

of HWs in response to ALL forcing changes simulated by models are in some agreement with observations, not only over China as a whole, but also over the individual subregions, though the magnitudes of the changes in the model are slightly different from the observed ones.

For the compound HWs, in response to ALL forcing, the area-averaged changes in frequency and intensity over the whole mainland China are 0.75 events per year and 1.07°C, which are about 2/3 of the observed 1.18 events per year and 1.67°C (Figs. 7a,b), and the change

in spatial extent over all of China is $3.54 \times 10^6 \, \text{km}^2$, very close to the $3.31 \times 10^6 \, \text{km}^2$ in observations (Fig. 7c). Moreover, the simulated increases in frequency (intensity) averaged over the SEC and WC are very similar to the observed changes, but increases in frequency (intensity) over the NEC are weaker than the observed changes. The simulated changes in spatial extent over the three subregions are also consistent with observations. Furthermore, the changes of GHG explain most responses in the simulated changes of compound HWs
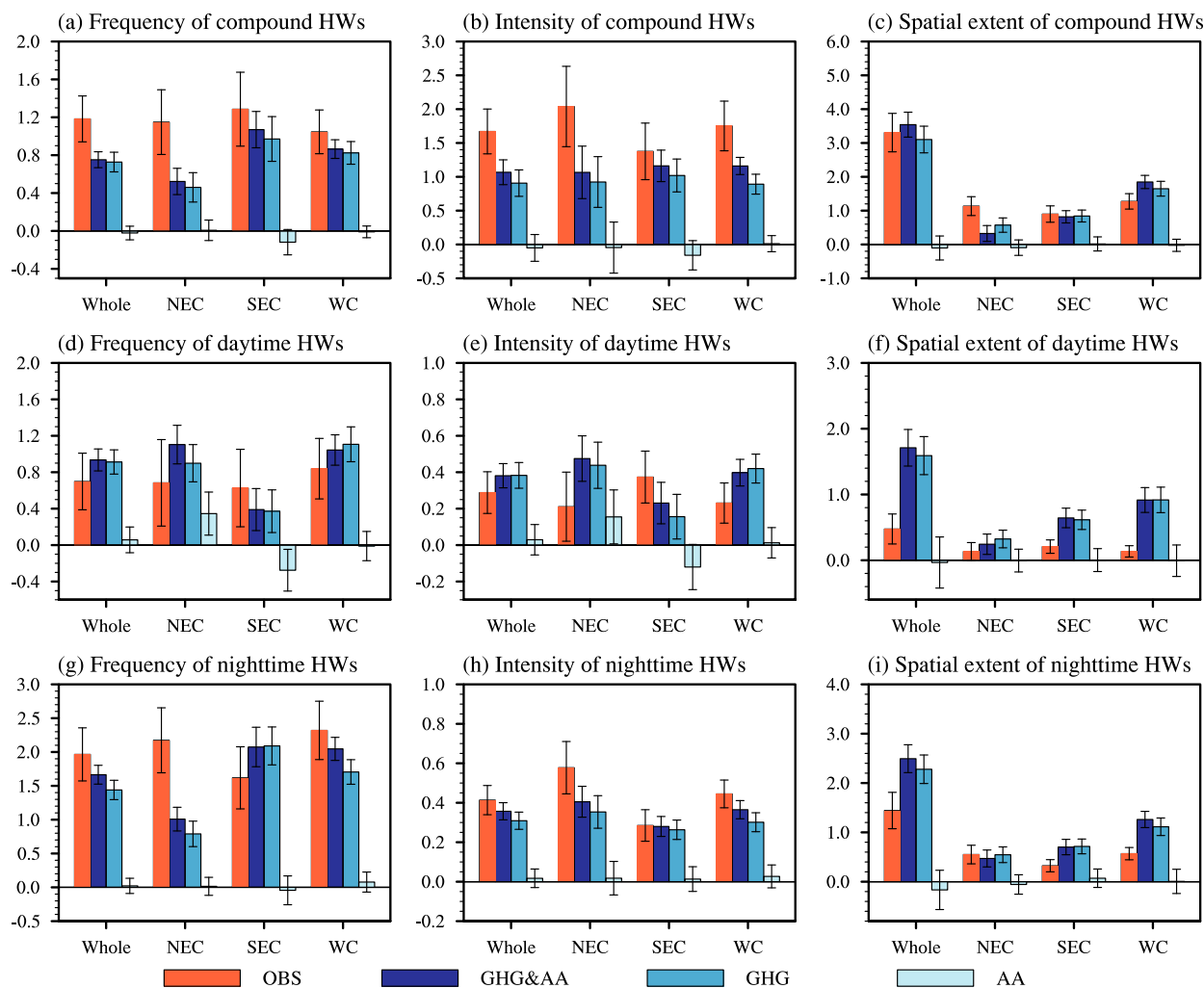
FIG. 7. Area-averaged changes in (left) frequency (events per year), (center) intensity (°C), and (right) spatial extent (km^2) of (a)–(c) compound, (d)–(f) daytime, and (g)–(i) nighttime HWs over all of China, NEC, SEC, and WC in observations and simulations forced by ALL forcing, GHG forcing, and AA forcing. The error bars indicate the 90% confidence intervals based on a two-tailed Student's t test.

over all of China or over the three subregions, indicating the predominant role of GHG changes in affecting the compound HWs.

For the daytime HWs, the changes in frequency and intensity averaged over all of China and the three subregions in the ALL forcing experiment are close to those in the observations, with simulated changes over all of China of 0.93 events per year and 0.38°C, compared to the observed ones of 0.70 events per year and 0.29°C (Figs. 7d,e). The simulated change in spatial extent is overestimated (Fig. 7f). Similar to the compound HWs, the area-averaged changes of the daytime HWs are primarily induced by the GHG changes. However, unlike the compound HWs, the changes of daytime HWs over the NEC and SEC are significantly influenced by the AA changes. The changes in frequency and intensity

of daytime HWs over the NEC in response to AA forcing are 0.35 events per year and 0.15°C, while they are −0.28 events per year and −0.12°C over the SEC. These significant increases over the NEC and decreases over the SEC are consistent with the dipole pattern of AA-induced changes in frequency and intensity (Figs. 5e,f).

For nighttime HWs, the simulated changes in most aspects agree well with the observed ones except that the change in frequency over NEC and the GHG changes play a key role in leading to the changes in frequency, intensity, and spatial extent. The changes in frequency and intensity of nighttime HWs averaged over all of China in response to ALL forcing are 1.66 events per year and 0.36°C, close to the 1.96 events per year and 0.41°C in observations (Figs. 7g,h). The

simulated change in spatial extent is greater than the observed changes in the whole region, SEC, and WC (Fig. 7i).

There is some nonlinearity in the changes in frequency and intensity for all three type HWs, especially strong for daytime HWs over the SEC in response to GHG and AA changes in model simulations, evidenced by the sum of the responses to separate GHG and AA forcing being not equal to the response to the ALL forcing. The nonlinearity is weak for changes of daytime HWs averaged over all of China and over two other subregions and all the area-averaged changes of compound and nighttime HWs. The nonlinearity of responses to different forcings has noticed by previous studies (Feichter et al. 2004; Ming and Ramaswamy 2009; Shiogama et al. 2013). However, detailed discussion of this nonlinearity is beyond the scope of this study.

The results above indicate that the observed decadal changes in the frequency, intensity, and spatial extent of compound, daytime, and nighttime HWs over China across the mid-1990s are primarily forced by the changes in anthropogenic forcings, such as GHG concentrations and AA emissions. The impacts of GHG changes and that of AA changes are different in many aspects. GHG changes contribute dominantly to the increases in all aspects of the three types of HWs over most regions in China, while AA changes significantly increase the frequency and intensity of the daytime HWs over NEC but decrease them over SEC.

5. Physical processes responsible for the simulated decadal changes of HWs

The physical processes responsible for the decadal changes of the three types of HWs in response to different forcings are discussed in this section by diagnosing the seasonal mean responses. The changes of HWs could be contributed by the changes in the climatological seasonal mean temperature and the changes in temperature variability. The contribution of changes in variability is estimated by calculating the properties of three types of HWs in the C-PD simulation by removing the climatological extended-summer T_{max} and T_{min} differences between the C-PD and C-EP simulations relative to the C-EP simulation and by comparing these new estimated changes with changes diagnosed from the original C-PD simulation relative to C-EP simulation. Results indicate that removing the climatological mean state change nearly eliminates changes (not shown) in all properties of the three types of HWs over China seen in response to ALL forcing. These indicate little contribution of changes in temperature variability and suggest that the decadal changes of the three types of

HWs in response to ALL forcing are predominantly attributed to the changes in the climatological seasonal mean temperature between the C-PD and C-EP simulations. This conclusion is in agreement with Argueso et al. (2016) who showed that seasonal mean temperature changes control future heat waves in most regions globally. Therefore, it is reasonable to examine the changes in the climatological seasonal mean state to discuss the associated physical processes.

a. Induced by GHG forcing

The spatial patterns of extended-summer-mean changes of some key variables in response to GHG changes are illustrated in Fig. 8. The increased downward clear-sky surface longwave (LW) radiation (6.01 W m^{-2} over NEC, 6.64 W m^{-2} over SEC, and 5.35 W m^{-2} over WC, Fig. 8a) indicates the warmer atmosphere induced by the increase in GHG concentrations via the greenhouse effect and related feedbacks. The downward surface clear-sky LW radiation increases more over SEC because of the greater increase of water vapor in the atmosphere (2.08 kg m^{-2} over SEC; Fig. 8b). The enhanced moisture transported from the South China Sea to SEC and moisture transport convergence (not shown) are responsible for moistening atmosphere over SEC. The enhanced moisture transport is induced by more water vapor evaporated from the warmer ocean and the southwesterly anomalies around the coast in SEC (Fig. 8d), which are related to the strengthened land–sea thermal contrast resulting from larger warming over land than over ocean (Fig. 8c). The enhanced moisture transport convergence over SEC is attributed to the increased moisture static energy related to more water vapor transport and the enhanced western North Pacific subtropical high (Fig. 8d) induced by the strengthened local Hadley circulation resulting from the increased tropical sea surface temperatures in response to GHG changes (Tian et al. 2018). These circulation and sea surface temperature responses are consistent with the previous studies (Lau and Kim 2017; Lau et al. 2017). The increase of net surface SW radiation is significant over NEC and WC (0.91 W m^{-2} over NEC and 2.06 W m^{-2} over WC; Fig. 8e), which warms the land surface in situ. The positive anomalies of the shortwave cloud radiative effect (SW CRE; 1.77 W m^{-2} over NEC and 1.75 W m^{-2} over WC; Fig. 8f) associated with the reduction of cloud cover over NEC and WC (Fig. 8g) result in the increased surface SW radiation. The reduction of cloud cover over NEC and WC is associated with a large decrease in relative humidity (Fig. 8h) since the water vapor in the atmosphere over land is mainly controlled by transport from the ocean and is constrained by ocean warming and increases less than saturation specific humidity following the Clausius–Clapeyron relationship because of stronger
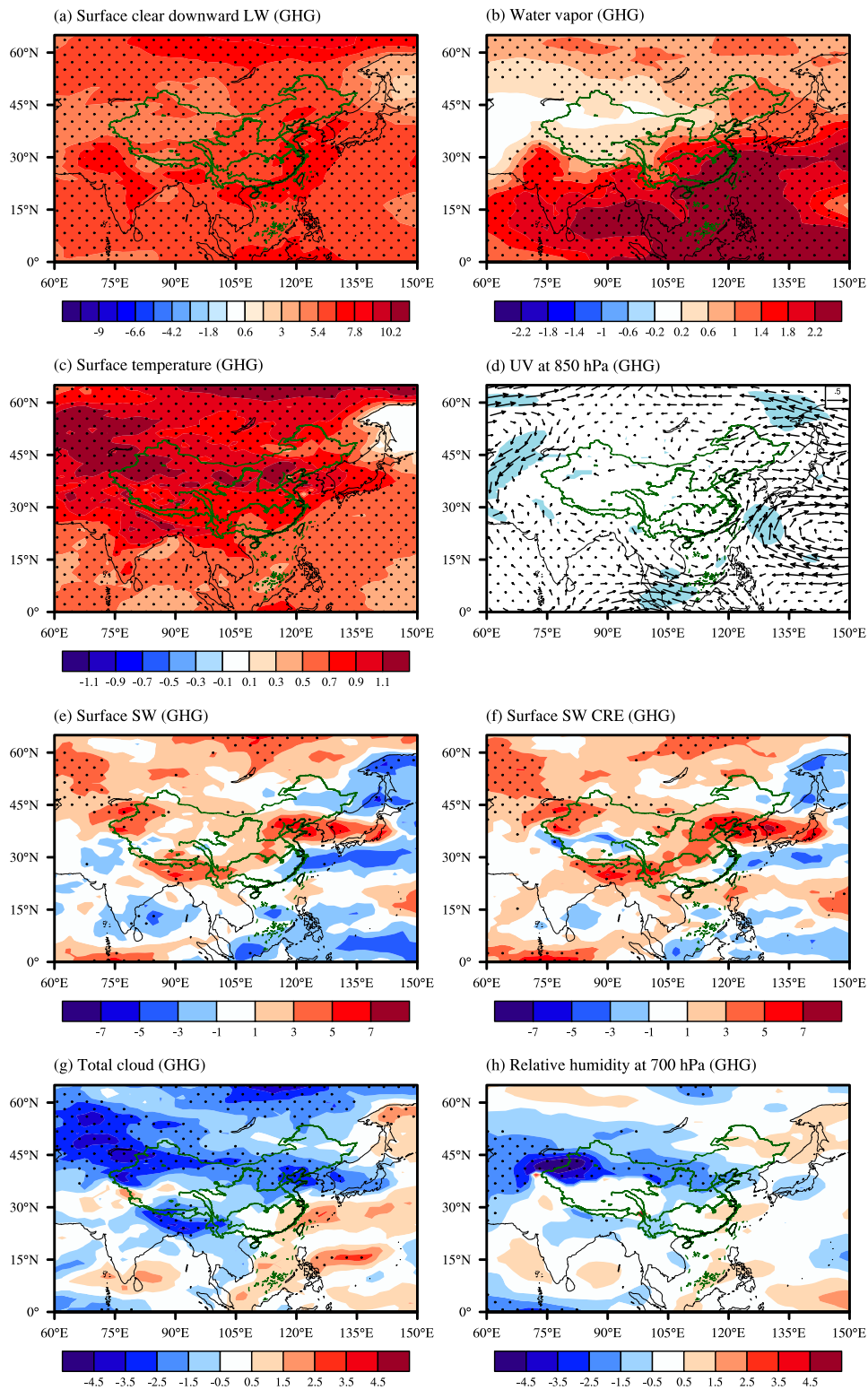
FIG. 8. Spatial patterns of extended-summer-mean response to changes in GHG forcing (C-PD-GHG minus C-EP): (a) surface clear-sky downward LW radiation (W m^{-2}); (b) water vapor (kg m^{-2}); (c) surface temperature (°C); (d) horizontal wind at 850 hPa (m s^{-1}); (e) net surface SW radiation (W m^{-2}); (f) surface SW CRE; (g) total cloud cover (%); and (h) relative humidity at 700 hPa (%). Positive values of radiation mean downward. The black dots in (a)–(c) and (e)–(h) and the blue shading in (d) highlight regions where the changes are statistically significant at the 90% confidence level based on a two-tailed Student's *t* test.

warming over land than over ocean (e.g., Dong et al. 2009; Boé and Terray 2014). In summary, the seasonal mean land surface and therefore surface air temperature (T_{max} and T_{min}) during extended summer increases directly by the strengthened greenhouse effect over all of China and indirectly by the positive LW feedback related to the increase in water vapor over SEC associated with circulation changes in response to GHG changes and by the positive SW feedback corresponding to the decrease in cloud cover over WC and NEC in which GHG change-induced warming in sea surface temperature plays an important role for the water vapor and circulation changes. As a result, all the frequency, intensity, and spatial extent of these three types of HWs are increased. Particularly, the positive LW feedback over SEC plays an important role in the increase in frequency of compound and nighttime HWs, while the positive SW feedback over WC and NEC dominates the increase in frequency of daytime HWs and the increase in intensity of all three types of HWs.

b. Induced by AA forcing

The spatial patterns of summer mean changes of some key variables in response to AA changes are illustrated in Fig. 9. The total aerosol optical depth (AOD) increases over most part of China (Fig. 9a), resulting in the reduction of the surface clear-sky SW radiation ($-2.97 \, W \, m^{-2}$ over China; Fig. 9b) through aerosol–radiation interaction, then leading to surface cooling. In particular, the surface air temperature over SEC ($-0.28°C$; Fig. 9h) decreases greatly because of the much larger decrease in surface SW radiation ($-6.37 \, W \, m^{-2}$ over SEC; Fig. 9c). However, although the AOD increases over NEC around 40°N, the surface SW radiation does not decrease much, because significant positive changes of SW CRE over NEC ($1.42 \, W \, m^{-2}$ over NEC; Fig. 9d) contributed to by the decrease in cloud cover (Fig. 9e) offset the decrease in surface clear-sky SW (Fig. 9b) and warm the surface air (Fig. 9h). The decrease in cloud cover is associated with the decrease in rainfall over NEC (Fig. 9f), which is featured by weakened EASM induced by the decreased land–sea thermal contrast and weakened atmospheric stability (Tian et al. 2018). In addition, Zhang et al. (2017) addressed that the increase in AA emission induces the increase in the frequency of summer drought over North China by using phase 5 of the Coupled Model Intercomparison Project (CMIP5) model simulations. Furthermore, the reduced precipitation over NEC leads to a decrease in soil moisture (Fig. 9g) and decrease in evaporation (not shown), reducing the upward latent heat fluxes (not shown). This increased SW radiation due to decreased cloud cover and the reduced upward latent heat fluxes due to decreased soil moisture and evaporation exert a positive feedback to warm the

surface and therefore surface air (Fig. 9h). Therefore, it is the decrease in surface clear-sky SW radiation related to the increase of AOD (Figs. 9a,b) that induces the decreases in frequency and intensity of daytime HWs over SEC through aerosol–radiation interaction. On the other hand, it is the increased SW CRE over NEC (Fig. 9d) related to weakened EASM overwhelming the decrease in clear-sky SW radiation (Fig. 9b) and the local precipitation–soil moisture–temperature interactions that jointly cause the increases in the frequency and intensity of daytime HWs over NEC.

6. Conclusions

The decadal changes across the mid-1990s of three types of HWs, that is, compound HWs, daytime HWs, and nighttime HWs, during extended summer (May–September) are detected on the aspects of frequency, intensity, and spatial extent by using the Chinese station dataset. A set of numerical time-sliced experiments is performed by an atmosphere–ocean–mixed layer coupled model to assess the role of anthropogenic forcings, including changes in GHG concentrations and AA emissions, in generating the decadal changes of the three types of HWs, and to evaluate the different contributions of individual GHG forcing and individual AA forcing to the HW decadal changes and to understand physical processes involved. The principle results are concluded as follows.

The three types of HWs over China experienced significant rapid decadal changes across the mid-1990s, noted by an increase in frequency, an enhancement in intensity, and an expansion in spatial extent. The compound HWs change most remarkably in all three aspects. The changes of daytime and nighttime HWs are also significant, though not as dramatic as changes of the compound HWs.

Results of the model simulations demonstrate that the anthropogenic forcing, including changes in GHG concentrations and AA emissions, has played a predominant role in generating the observed decadal changes in the frequency, intensity, and spatial extent of the three types of HWs. The spatial patterns of changes of the three types of HWs are well reproduced by the atmosphere–ocean–mixed layer coupled model MetUM-GOML1 in response to changes in GHG and AA forcings together (ALL forcing). Quantitatively, simulated changes in frequency and intensity over China and over three subregions in response to ALL forcing are also comparable to the observed changes.

Individually, GHG changes dominantly result in the simulated changes of the three types of HWs in response to ALL forcing, while AA changes make a relatively
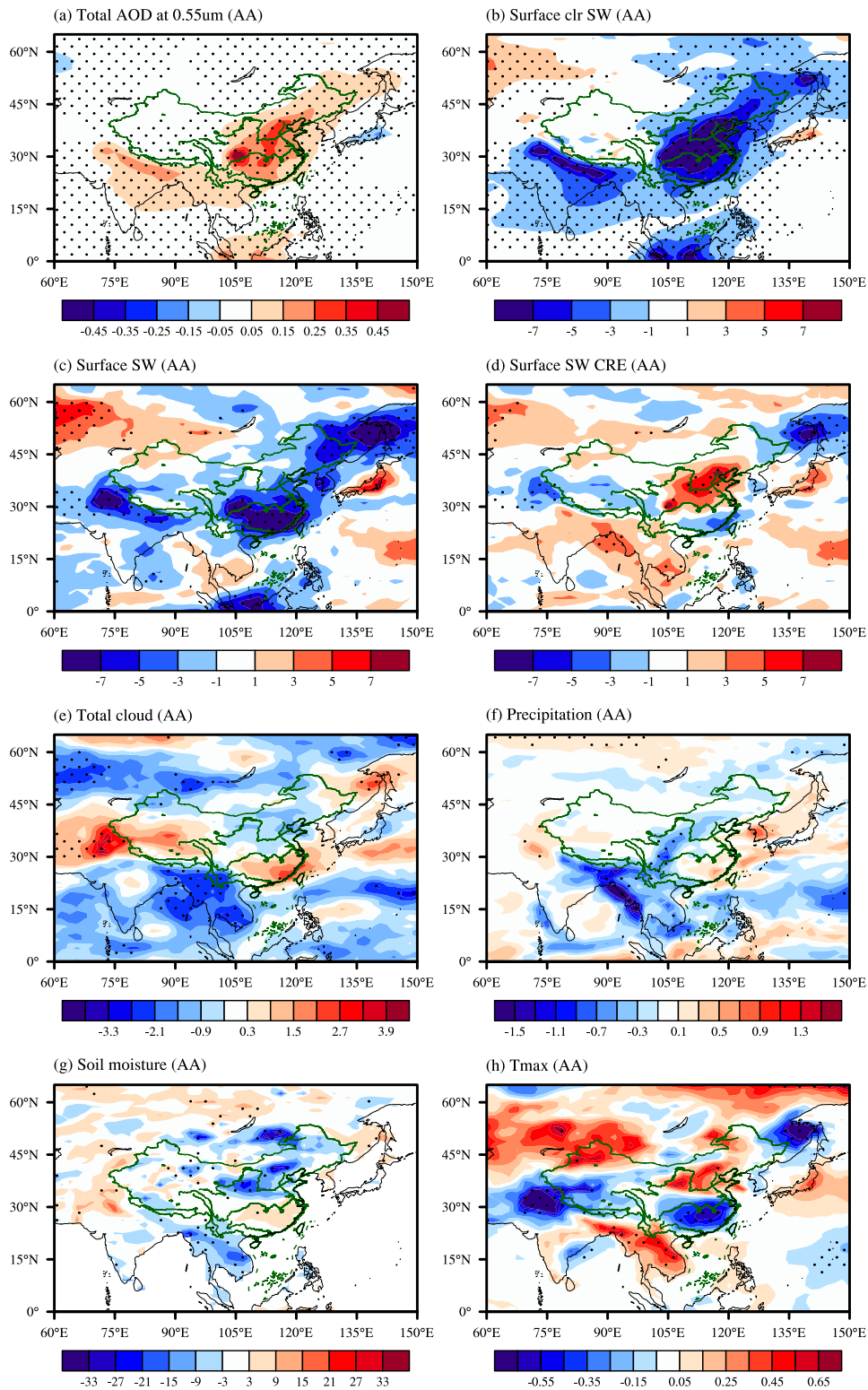
FIG. 9. Spatial patterns of extended-summer-mean response to changes in AA forcing (C-PD-AA minus C-EP): (a) total AOD at 0.55 μm; (b) net clear-sky surface SW radiation (W m^{-2}); (c) net surface SW radiation (W m^{-2}); (d) surface SW CRE; (e) total cloud cover (%); (f) precipitation (mm day^{-1}); (g) soil moisture (kg m^{-2}); and (h) T_{max} (°C). Positive values of radiation mean downward. The black dots highlight regions where the changes are statistically significant at the 90% confidence level based on a two-tailed Student's t test.

weak contribution, and the changes in GHG and AA forcing have distinct impacts on the changes of the three types of HWs. Changes in GHG concentrations play a crucial role in increasing the frequency, intensity, and spatial extent of all three types of HWs over China. Changes in AA emissions have a weak influence on compound and nighttime HWs. However, AA changes significantly increase the frequency and intensity of daytime HWs over NEC and decrease them over SEC.

The GHG changes increase the frequency, intensity, and spatial extent of the three types of HWs both directly via the strengthened greenhouse effect and indirectly via atmosphere and circulation feedbacks in which GHG change-induced warming in sea surface temperature plays an important role. Over the subregions of WC and NEC, the warmer atmosphere due to the increase in GHG concentrations, accompanied by limited increase in water vapor in the atmosphere, results in the reduction of cloud cover. Increased surface downward SW radiation, resulting from positive SW cloud radiative effect over WC and NEC, heats the surface and warms the surface air as a positive feedback. Over the subregion of SEC, the increase of water vapor in the atmosphere—induced by the enhanced moisture transport and moisture transport convergence over SEC due to the circulation changes and warming in sea surface temperature in response to GHG changes—has a positive feedback on surface warming.

The AA changes significantly decrease the frequency and intensity of daytime HWs over SEC through aerosol–radiation interaction and increase them over NEC by the AA change-induced rainfall change and atmosphere–surface feedbacks related to the weakened East Asian summer monsoon. Increased AOD over the eastern part of China directly reduces the surface SW radiation and decreases the surface temperature and surface air temperature over SEC and therefore the frequency and intensity of daytime HWs. Reduced cloud cover over NEC, resulting from the decrease in convection in response to AA changes, increases the surface SW radiation and warms the surface and surface air. The reduced rainfall also leads to decreased upward latent heat fluxes due to decreased soil moisture, which—combined with the increased SW radiation related to less cloud cover—tends to warm the surface. These surface feedbacks overwhelm the direct cooling impact induced by the increase in AA emissions and lead to increases in the frequency and intensity of daytime HWs over NEC.

The results demonstrate the dominant contributions of anthropogenic changes, especially the increased GHG concentrations, to the observed decadal changes in frequency, intensity, and spatial extent of the three

types of HWs over China during extended summer across the mid-1990s. The GHG changes raise the mean surface air temperature and air-column temperature, increasing all the aspects of the three types of HWs over nearly all of China with important water vapor feedbacks associated with GHG-induced sea surface temperature changes. The AA changes have different local impacts. Local interaction between reduced precipitation, cloud cover, soil moisture, evaporation, and temperature related to a weakened East Asian summer monsoon play an important role in warming the surface atmosphere over NEC and therefore changing the properties of daytime HWs.

Looking for a few decades ahead, GHGs will continue to increase while aerosol emissions over China are expected to decrease. China will experience more HWs of different types over different regions with greater severity, and the areas affected by severe HWs will also be expanded. Therefore, better strategies for adaptation and mitigation against different types of HWs over different regions would benefit the people and society.

This paper primarily investigates the individual roles of GHG concentrations and AA emissions in the decadal change of the three types of HWs over China. There are some other factors that could affect the decadal change of HWs over China, such as land-use and land-cover change (Findell et al. 2017; Li et al. 2018a) and the phase shift of the Atlantic multidecadal oscillation, which might have contributed to warming over the Eurasian continent around the mid-1990s (Hong et al. 2017). More effort is needed to quantify their contributions to the recent decadal changes of HWs over China.

Moreover, the responses to AA forcing are influenced not only by the AA emissions, but also by climatology, aerosol transport and deposition, and chemical processes in the model. All these processes affect the distribution of the aerosol burden (e.g., Wilcox et al. 2015b) and suggest a possible model dependence of the responses to AA forcing. Wang et al. (2019) pointed out that there is a large intermodel spread of responses to AA forcings in different climate models. The model dependence and intermodel uncertainty of the responses call for improved models to investigate the responses to AA forcings.

REFERENCES

Alexander, L. V., and Coauthors, 2006: Global observed changes in daily climate extremes of temperature and precipitation. *J. Geophys. Res.*, **111**, D05109, https://doi.org/10.1029/2005JD006290.

Argueso, D., A. Di Luca, S. Perkins-Kirkpatrick, and J. P. Evans, 2016: Seasonal mean temperature changes control future heat waves. *Geophys. Res. Lett.*, **43**, 7653–7660, https://doi.org/10.1002/2016GL069408.

Arribas, A., and Coauthors, 2011: The GloSea4 ensemble prediction system for seasonal forecasting. *Mon. Wea. Rev.*, **139**, 1891–1910, https://doi.org/10.1175/2010MWR3615.1.

Boé, J., and L. Terray, 2014: Land–sea contrast, soil–atmosphere and cloud–temperature interactions: Interplays and roles in future summer European climate change. *Climate Dyn.*, **42**, 683–699, https://doi.org/10.1007/s00382-013-1868-8.

Chen, W., and B. Dong, 2019: Anthropogenic impacts on recent decadal change in temperature extremes over China: Relative roles of greenhouse gases and anthropogenic aerosols. *Climate Dyn.* **52**, 3643–3660, https://doi.org/10.1007/s00382-018-4342-9.

Chen, Y., and Y. Li, 2017: An inter-comparison of three heat wave types in China during 1961-2010: Observed basic features and linear trends. *Sci. Rep.*, **7**, 45619, https://doi.org/10.1038/srep45619.

——, and P. Zhai, 2017: Revisiting summertime hot extremes in China during 1961–2015: Overlooked compound extremes and significant changes. *Geophys. Res. Lett.*, **44**, 5096–5103, https://doi.org/10.1002/2016gl072281.

Coumou, D., and S. Rahmstorf, 2012: A decade of weather extremes. *Nat. Climate Change*, **2**, 491–496, https://doi.org/10.1038/nclimate1452.

Cubasch, U., and Coauthors, 2001: Projections of future climate change. *Climate Change 2001: The Scientific Basis*, J. T. Houghton et al., Eds., Cambridge University Press, 526–582.

Della-Marta, P. M., J. Luterbacher, H. von Weissenfluh, E. Xoplaki, M. Brunet, and H. Wanner, 2007: Summer heat waves over western Europe 1880–2003, their relationship to large-scale forcings and predictability. *Climate Dyn.*, **29**, 251–275, https://doi.org/10.1007/s00382-007-0233-1.

Ding, T., W. H. Qian, and Z. W. Yan, 2010: Changes in hot days and heat waves in China during 1961–2007. *Int. J. Climatol.*, **30**, 1452–1462, https://doi.org/10.1002/joc.1989.

Donat, M. G., and Coauthors, 2013: Updated analyses of temperature and precipitation extreme indices since the beginning of the twentieth century: The HadEX2 dataset. *J. Geophys. Res. Atmos.*, **118**, 2098–2118, https://doi.org/10.1002/jgrd.50150.

Dong, B., J. M. Gregory, and R. T. Sutton, 2009: Understanding land–sea warming contrast in response to increasing greenhouse gases. Part I: Transient adjustment. *J. Climate*, **22**, 3079–3097, https://doi.org/10.1175/2009JCLI2652.1.

——, R. T. Sutton, E. J. Highwood, and L. J. Wilcox, 2016a: Preferred response of the East Asian summer monsoon to local and non-local anthropogenic sulphur dioxide emissions.

Climate Dyn., **46**, 1733–1751, https://doi.org/10.1007/s00382-015-2671-5.

——, ——, W. Chen, X. Liu, R. Lu, and Y. Sun, 2016b: Abrupt summer warming and changes in temperature extremes over northeast Asia since the mid-1990s: Drivers and physical processes. *Adv. Atmos. Sci.*, **33**, 1005–1023, https://doi.org/10.1007/s00376-016-5247-3.

——, ——, L. Shaffrey, and N. P. Klingaman, 2017: Attribution of forced decadal climate change in coupled and uncoupled ocean–atmosphere model experiments. *J. Climate*, **30**, 6203–6223, https://doi.org/10.1175/JCLI-D-16-0578.1.

Feichter, J., E. Roeckner, U. Lohmann, and B. Liepert, 2004: Nonlinear aspects of the climate response to greenhouse gas and aerosol forcing. *J. Climate*, **17**, 2384–2398, https://doi.org/10.1175/1520-0442(2004)017<2384:NAOTCR>2.0.CO;2.

Findell, K. L., A. Berg, P. Gentine, J. P. Krasting, B. R. Lintner, S. Malyshev, J. A. Santanello, and E. Shevliakova, 2017: The impact of anthropogenic land use and land cover change on regional climate extremes. *Nat. Commun.*, **8**, 989, https://doi.org/10.1038/s41467-017-01038-w.

Fischer, E. M., S. I. Seneviratne, P. L. Vidale, D. Lüthi, and C. Schär, 2007: Soil moisture–atmosphere interactions during the 2003 European summer heat wave. *J. Climate*, **20**, 5081–5099, https://doi.org/10.1175/JCLI4288.1.

Freychet, N., S. Tett, J. Wang, and G. Hegerl, 2017: Summer heat waves over Eastern China: Dynamical processes and trend attribution. *Environ. Res. Lett.*, **12**, 024015, https://doi.org/10.1088/1748-9326/aa5ba3.

——, ——, G. Hegerl, and J. Wang, 2018a: Central-Eastern China persistent heat waves: Evaluation of the AMIP models. *J. Climate*, **31**, 3609–3624, https://doi.org/10.1175/JCLI-D-17-0480.1.

——, S. Sparrow, S. F. B. Tett, M. J. Mineter, G. C. Hegerl, and D. C. H. Wallom, 2018b: Impacts of anthropogenic forcings and El Niño on Chinese extreme temperatures. *Adv. Atmos. Sci.*, **35**, 994–1002, https://doi.org/10.1007/s00376-018-7258-8.

Gosling, S. N., J. A. Lowe, G. R. McGregor, M. Pelling, and B. D. Malamud, 2009: Associations between elevated atmospheric temperature and human mortality: A critical review of the literature. *Climatic Change*, **92**, 299–341, https://doi.org/10.1007/s10584-008-9441-x.

Guo, L., E. J. Highwood, L. C. Shaffrey, and A. G. Turner, 2013: The effect of regional changes in anthropogenic aerosols on rainfall of the East Asian summer monsoon. *Atmos. Chem. Phys.*, **13**, 1521–1534, https://doi.org/10.5194/acp-13-1521-2013.

Guo, X., J. Huang, Y. Luo, Z. Zhao, and Y. Xu, 2017: Projection of heat waves over China for eight different global warming targets using 12 CMIP5 models. *Theor. Appl. Climatol.*, **128**, 507–522, https://doi.org/10.1007/s00704-015-1718-1.

Hajat, S., and Coauthors, 2006: Impact of high temperatures on mortality: Is there an added heat wave effect? *Epidemiology*, **17**, 632–638, https://doi.org/10.1097/01.ede.0000239688.70829.63.

Hirons, L., N. Klingaman, and S. Woolnough, 2015: MetUM-GOML: A near-globally coupled atmosphere–ocean-mixed-layer model. *Geosci. Model Dev.*, **8**, 363–379, https://doi.org/10.5194/gmd-8-363-2015.

Hong, J. S., S. W. Yeh, and K. H. Seo, 2018: Diagnosing physical mechanisms leading to pure heat waves versus pure tropical nights over the Korean Peninsula. *J. Geophys. Res. Atmos.*, **123**, 7149–7160, https://doi.org/10.1029/2018jd028360.

Hong, X., R. Lu, and S. Li, 2017: Amplified summer warming in Europe–west Asia and northeast Asia after the mid-1990s. *Environ. Res. Lett.*, **12**, 094007, https://doi.org/10.1088/1748-9326/aa7909.

Jones, P. D., S. C. B. Raper, R. S. Bradley, H. F. Diaz, P. M. Kelly, and T. M. L. Wigley, 1986: Northern Hemisphere surface air temperature variations: 1851–1984. *J. Climate Appl. Meteor.*, **25**, 161–179, https://doi.org/10.1175/1520-0450(1986)025<0161: NHSATV>2.0.CO;2.

Lamarque, J.-F., and Coauthors, 2010: Historical (1850–2000) gridded anthropogenic and biomass burning emissions of reactive gases and aerosols: Methodology and application. *Atmos. Chem. Phys.*, **10**, 7017–7039, https://doi.org/10.5194/acp-10-7017-2010.

——, G. P. Kyle, M. Meinshausen, K. Riahi, S. J. Smith, D. P. van Vuuren, A. J. Conley, and F. Vitt, 2011: Global and regional evolution of short-lived radiatively-active gases and aerosols in the representative concentration pathways. *Climatic Change*, **109**, 191, https://doi.org/10.1007/s10584-011-0155-0.

Lau, W. K. M., and K. M. Kim, 2017: Competing influences of greenhouse warming and aerosols on Asian summer monsoon circulation and rainfall. *Asia-Pac. J. Atmos. Sci.*, **53**, 181–194, https://doi.org/10.1007/s13143-017-0033-4.

——, ——, and L. R. Leung, 2017: Changing circulation structure and precipitation characteristics in Asian monsoon regions: Greenhouse warming vs. aerosol effects. *Geosci. Lett.*, **4**, 28, https://doi.org/10.1186/s40562-017-0094-3.

Le Quéré, C., and Coauthors, 2009: Trends in the sources and sinks of carbon dioxide. *Nat. Geosci.*, **2**, 831, https://doi.org/10.1038/ngeo689.

Li, X., and M. Ting, 2017: Understanding the Asian summer monsoon response to greenhouse warming: The relative roles of direct radiative forcing and sea surface temperature change. *Climate Dyn.*, **49**, 2863–2880, https://doi.org/10.1007/s00382-016-3470-3.

——, H. Chen, J. Wei, W. Hua, S. Sun, H. Ma, X. Li, and J. Li, 2018a: Inconsistent responses of hot extremes to historical land use and cover change among the selected CMIP5 models. *J. Geophys. Res. Atmos.*, **123**, 3497–3512, https://doi.org/10.1002/2017jd028161.

——, M. Ting, and D. E. Lee, 2018b: Fast adjustments of the Asian summer monsoon to anthropogenic aerosols. *Geophys. Res. Lett.*, **45**, 1001–1010, https://doi.org/10.1002/2017GL076667.

Li, Y., Y. Ding, and W. Li, 2017: Observed trends in various aspects of compound heat waves across China from 1961 to 2015. *J. Meteor. Res.*, **31**, 455–467, https://doi.org/10.1007/s13351-017-6150-2.

Li, Z., L. J. Cao, Y. N. Zhu, and Z. W. Yan, 2016a: Comparison of two homogenized datasets of daily maximum/mean/minimum temperature in China during 1960-2013. *J. Meteor. Res.*, **30**, 53–66, https://doi.org/10.1007/s13351-016-5054-x.

——, and Coauthors, 2016b: Aerosol and monsoon climate interactions over Asia. *Rev. Geophys.*, **54**, 866–929, https://doi.org/10.1002/2015RG000500.

Lu, C. H., Y. Sun, H. Wan, X. B. Zhang, and H. Yin, 2016: Anthropogenic influence on the frequency of extreme temperatures in China. *Geophys. Res. Lett.*, **43**, 6511–6518, https://doi.org/10.1002/2016GL069296.

Lu, R. Y., and R. D. Chen, 2016: A review of recent studies on extreme heat in China. *Atmos. Ocean. Sci. Lett.*, **9**, 114–121, https://doi.org/10.1080/16742834.2016.1133071.

Luo, F., B. Dong, F. Tian, and S. Li, 2019: Anthropogenically forced decadal change of South Asian summer monsoon across the mid-1990s. *J. Geophys. Res. Atmos.*, **124**, 806–824, https://doi.org/10.1029/2018JD029195.

Luo, M., and N.-C. Lau, 2017: Heat waves in southern China: Synoptic behavior, long-term change, and urbanization

effects. *J. Climate*, **30**, 703–720, https://doi.org/10.1175/JCLI-D-16-0269.1.

Ma, S. M., T. J. Zhou, D. A. Stone, O. Angelil, and H. Shiogama, 2017: Attribution of the July–August 2013 heat event in central and eastern China to anthropogenic greenhouse gas emissions. *Environ. Res. Lett.*, **12**, 054020, https://doi.org/10.1088/1748-9326/aa69d2.

Matsueda, M., 2011: Predictability of Euro-Russian blocking in summer of 2010. *Geophys. Res. Lett.*, **38**, L06801, https://doi.org/10.1029/2010GL046557.

Meehl, G. A., and C. Tebaldi, 2004: More intense, more frequent, and longer lasting heat waves in the 21st century. *Science*, **305**, 994–997, https://doi.org/10.1126/science.1098704.

Ming, Y., and V. Ramaswamy, 2009: Nonlinear climate and hydrological responses to aerosol effects. *J. Climate*, **22**, 1329–1339, https://doi.org/10.1175/2008JCLI2362.1.

Perkins, S. E., 2015: A review on the scientific understanding of heatwaves—Their measurement, driving mechanisms, and changes at the global scale. *Atmos. Res.*, **164–165**, 242–267, https://doi.org/10.1016/j.atmosres.2015.05.014.

——, and L. V. Alexander, 2013: On the measurement of heat waves. *J. Climate*, **26**, 4500–4517, https://doi.org/10.1175/JCLI-D-12-00383.1.

Rayner, N. A., D. E. Parker, E. B. Horton, C. K. Folland, L. V. Alexander, D. P. Rowell, E. C. Kent, and A. Kaplan, 2003: Global analyses of sea surface temperature, sea ice, and night marine air temperature since the late nineteenth century. *J. Geophys. Res.*, **108**, 4407, https://doi.org/10.1029/2002JD002670.

Robine, J.-M., S. L. K. Cheung, S. Le Roy, H. Van Oyen, C. Griffiths, J.-P. Michel, and F. R. Herrmann, 2008: Death toll exceeded 70,000 in Europe during the summer of 2003. *C. R. Biol.*, **331**, 171–178, https://doi.org/10.1016/j.crvi.2007.12.001.

Rosenfeld, D., U. Lohmann, G. B. Raga, C. D. O'Dowd, M. Kulmala, S. Fuzzi, A. Reissell, and M. O. Andreae, 2008: Flood or drought: How do aerosols affect precipitation? *Science*, **321**, 1309–1313, https://doi.org/10.1126/science.1160606.

Schär, C., and G. Jendritzky, 2004: Climate change: Hot news from summer 2003. *Nature*, **432**, 559, https://doi.org/10.1038/432559a.

Seneviratne, S. I., M. G. Donat, B. Mueller, and L. V. Alexander, 2014: No pause in the increase of hot temperature extremes. *Nat. Climate Change*, **4**, 161, https://doi.org/10.1038/nclimate2145.

Shiogama, H., D. A. Stone, T. Nagashima, T. Nozawa, and S. Emori, 2013: On the linear additivity of climate forcing-response relationships at global and continental scales. *Int. J. Climatol.*, **33**, 2542–2550, https://doi.org/10.1002/joc.3607.

Smith, D. M., and J. M. Murphy, 2007: An objective ocean temperature and salinity analysis using covariances from a global climate model. *J. Geophys. Res.*, **112**, C02022, https://doi.org/10.1029/2005JC003172.

Stefanon, M., D. A. Fabio, and D. Philippe, 2012: Heatwave classification over Europe and the Mediterranean region. *Environ. Res. Lett.*, **7**, 014023, https://doi.org/10.1088/1748-9326/7/1/014023.

Stevens, B., and G. Feingold, 2009: Untangling aerosol effects on clouds and precipitation in a buffered system. *Nature*, **461**, 607–613, https://doi.org/10.1038/nature08281.

Sun, Y., X. B. Zhang, F. W. Zwiers, L. C. Song, H. Wan, T. Hu, H. Yin, and G. Y. Ren, 2014: Rapid increase in the risk to extreme summer heat in Eastern China. *Nat. Climate Change*, **4**, 1082–1085, https://doi.org/10.1038/nclimate2410.

——, L. Song, H. Yin, B. Zhou, T. Hu, X. Zhang, and P. Stott, 2016: Human influence on the 2015 extreme high temperature

events in Western China [in "Explaining Extremes of 2015 from a Climate Perspective"]. *Bull. Amer. Meteor. Soc.*, **97** (12), S102–S106, https://doi.org/10.1175/BAMS-D-16-0158.1.

Tan, J., Y. Zheng, G. Song, L. S. Kalkstein, A. J. Kalkstein, and X. Tang, 2007: Heat wave impacts on mortality in Shanghai, 1998 and 2003. *Int. J. Biometeor.*, **51**, 193–200, https://doi.org/10.1007/s00484-006-0058-3.

Tao, W. K., J. P. Chen, Z. Li, C. Wang, and C. Zhang, 2012: Impact of aerosols on convective clouds and precipitation. *Rev. Geophys.*, **50**, RG2001, https://doi.org/10.1029/2011RG000369.

Tian, F., B. Dong, J. Robson, and R. Sutton, 2018: Forced decadal changes in the East Asian summer monsoon: The roles of greenhouse gases and anthropogenic aerosols. *Climate Dyn.*, **51**, 3699–3715, https://doi.org/10.1007/s00382-018-4105-7.

Walters, D., and Coauthors, 2011: The Met Office Unified Model global atmosphere 3.0/3.1 and JULES global land 3.0/3.1 configurations. *Geosci. Model Dev.*, **4**, 919–941, https://doi.org/10.5194/gmd-4-919-2011.

Wang, H., S. Xie, Y. Kosaka, Q. Liu, and Y. Du, 2019: Dynamics of Asian summer monsoon response to anthropogenic aerosol forcing. *J. Climate*, **32**, 843–858, https://doi.org/10.1175/jcli-d-18-0386.1.

Wang, P., J. Tang, X. Sun, S. Wang, J. Wu, X. Dong, and J. Fang, 2017: Heat waves in China: Definitions, leading patterns, and connections to large-scale atmospheric circulation and SSTs. *J. Geophys. Res. Atmos.*, **122**, 10 679–10 699, https://doi.org/10.1002/2017JD027180.

Wen, Q. Z. H., X. B. Zhang, Y. Xu, and B. Wang, 2013: Detecting human influence on extreme temperatures in China. *Geophys. Res. Lett.*, **40**, 1171–1176, https://doi.org/10.1002/grl.50285.

Wilcox, L. J., B. Dong, R. T. Sutton, and E. J. Highwood, 2015a: The 2014 hot, dry summer in northeast Asia [in "Explaining Extremes of 2014 from a Climate Perspective"]. *Bull. Amer. Meteor. Soc.*, **96** (12), S105–S110, https://doi.org/10.1175/BAMS-D-15-00123.1.

——, E. J. Highwood, B. B. B. Booth, and K. S. Carslaw, 2015b: Quantifying sources of inter-model diversity in the cloud albedo effect. *Geophys. Res. Lett.*, **42**, 1568–1575, https://doi.org/10.1002/2015GL063301.

Yin, H., Y. Sun, H. Wan, X. B. Zhang, and C. H. Lu, 2017: Detection of anthropogenic influence on the intensity of extreme temperatures in China. *Int. J. Climatol.*, **37**, 1229–1237, https://doi.org/10.1002/joc.4771.

You, Q. L., Z. H. Jiang, L. Kong, Z. W. Wu, Y. T. Bao, S. C. Kang, and N. Pepin, 2017: A comparison of heat wave climatologies and trends in China based on multiple definitions. *Climate Dyn.*, **48**, 3975–3989, https://doi.org/10.1007/s00382-016-3315-0.

Zhang, L. X., P. L. Wu, and T. J. Zhou, 2017: Aerosol forcing of extreme summer drought over North China. *Environ. Res. Lett.*, **12**, https://doi.org/10.1088/1748-9326/aa5fb3.

Zhou, T. J., S. M. Ma, and L. W. Zou, 2014: Understanding a hot summer in Central Eastern China: Summer 2013 in context of multimodel trend analysis [in "Explaining Extremes of 2013 from a Climate Perspective"]. *Bull. Amer. Meteor. Soc.*, **95** (9), S54–S57.